Naturwissenschaften (2000) 87:423–438

REVIEW ARTICLE

D. Goll · H. Kronmüller

High-performance permanent magnets

Abstract High-performance permanent magnets (pms) are based on compounds with outstanding intrinsic magnetic properties as well as on optimized microstructures and alloy compositions. The most powerful pm materials at present are RE–TM intermetallic alloys which derive their exceptional magnetic properties from the favourable combination of rare earth metals (RE = Nd, Pr, Sm) with transition metals (TM = Fe, Co), in particular magnets based on $(Nd,Pr)_2Fe_{14}B$ and $Sm_2(Co,Cu,Fe,Zr)_{17}$. Their development during the last 20 years has involved a dramatic improvement in their performance by a factor of >15 compared with conventional ferrite pms therefore contributing positively to the ever-increasing demand for pms in many (including new) application fields, to the extent that RE–TM pms now account for nearly half of the worldwide market. This review article first gives a brief introduction to the basics of ferromagnetism to confer an insight into the variety of (permanent) magnets, their manufacture and application fields. We then examine the rather complex relationship between the microstructure and the magnetic properties for the two highest-performance and most promising pm materials mentioned. By using numerical micromagnetic simulations on the basis of the Finite Element technique the correlation can be quantitatively predicted, thus providing a powerful tool for the further development of optimized high-performance pms.

Introduction

Never before has our daily environment been so significantly dependent on materials with outstanding magnetic properties. Whether for (motive) power, electrical, automotive and mechanical engineering, for computer, magnetic recording and telecommunication technology, for navigation, aviation and space operations, automation, medicine, sensors, precision mechanics or household appliances, we cannot imagine modern life in today's automated world without ferro- and ferrimagnetic materials.

On an atomic scale, ferromagnetism and ferrimagnetism have their origins predominantly in the spin magnetic moments but also in the orbital magnetic moments of their atomic electrons. These moments arise from the self rotation of the electrons about their own axes, i.e. the spin motion, and the orbital motion of the electrons around the atomic cores, respectively, adding themselves vectorially to the magnetic moment of the atom. In the case of the transition metals (Fe, Co and Ni), the orbital moments more or less vanish because of the so-called "quenching" of the orbital motion of the 3d electrons whereas in the case of the rare earth metals, the spin moments and the orbital moments are additive according to Hund's rules (Hund 1925). Because of the quantum mechanical exchange forces, neighbouring atomic moments are aligned in parallel in the case of ferromagnetic substances whereas in ferrimagnetic materials two different substructures occur whose moments are different in size and coupled antiparallel. In both cases, the ordering extends over ranges containing large numbers of atoms.

On a continuum scale, the alignment leads to the presence of a spontaneous polarization $\boldsymbol{J}_\mathbf{S}$ which represents the mean magnetic moment $\boldsymbol{m}$ per unit volume $V(\boldsymbol{J}_\mathbf{S} = \mu_0(\sum \boldsymbol{m})/V)$ with μ_0 corresponding to the vacuum permeability $\mu_0 = 4\pi \cdot 10^{-7}\ Vs/Am$) and depending on the temperature. As the temperature increases, the ordering is more and more disturbed by thermal agitation up to the Curie temperature T_C at which the phenomena ferromagnetism and ferrimagnetism disappear. In general, $\boldsymbol{J}_\mathbf{S}$ is uniform within so-called magnetic domains but not throughout a sample of macroscopic dimensions. To an external field $\boldsymbol{H}$, a bulk sample reacts

D. Goll (✉) · H. Kronmüller
Max-Planck-Institut für Metallforschung, Heisenbergstrasse 1, 70569 Stuttgart, Germany
e-mail: goll@vaxph.mpi-stuttgart.mpg.de
Tel.: +49-711-6891814

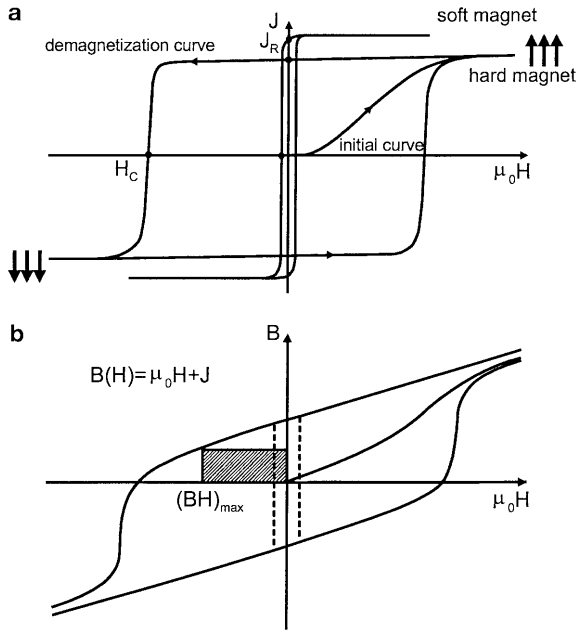

Fig. 1 Hysteresis loops: **a** J versus $\mu_0 H$ for typical soft and hard magnetic materials (the *arrows* reflect the orientation of the spins in the saturated state); and **b** B versus $\mu_0 H$ of a permanent magnet with $\mu_0 H_C > 0.5 J_R$ (*solid line*) and $\mu_0 H_C < 0.5 J_R$ (*dotted line*)

with a magnetic polarization ***J*** in a nonlinear manner. This correlation is represented by a plot of the hysteresis loop obtained by applying a magnetic field $\mu_0 H$ to the specimen and measuring the ensuing change of the magnetic polarization J in field direction (see Fig. 1a). Starting from the initial (demagnetized) state ($J = \mu_0 H = 0$) the polarization increases with an increase of the field along the initial magnetization curve and finally reaches the saturation polarization ($J = J_{sat}$). When the magnetizing field is reduced to zero from the saturated state the sample remains magnetized. This polarization at zero field is called the remanence J_R. It can be returned to zero by applying a reverse magnetic field of strength $\mu_0 H_C$ known as the coercive field which is therefore the measure for the magnet's resistance against demagnetizing fields. Further increase of the reversed applied field magnetizes the sample to saturation in the opposite direction ($J = -J_{sat}$).

The characteristics of the hysteresis loop determine the suitability of ferromagnetic (including ferrimagnetic) materials for a given application. In principle, ferromagnetic substances can be classified into soft and hard magnetic materials depending on how easily the material can be (de-)magnetized as shown in Fig. 1a.

Soft magnets (e.g. Fe) alloys based on Fe–Si, Fe–Ni (permalloy) and Fe–Co, soft ferrites and metallic glasses are characterized by low coercivity ($\mu_0 H_C < 1.25\ mT$) and high permeability $\mu = (\mu_0 H + J)/H$ ($10^5 \sim 10^6$) which enables such materials to amplify the flux produced by an electrical current considerably. On the other hand, the permeability of hard or permanent magnets (pms) is rather low. They provide stable permanent magnetic fields and create surface poles without continuous expenditure of electrical energy. For hard magnetic materials (e.g. RE–TM compounds, hard ferrites and AlNiCo), high coercivity ($\mu_0 H_C \approx 0.5$–$4\ T$), high remanence and a high maximum energy product are prime requirements. The maximum energy product $(BH)_{max}$ represents the magnetic energy per unit volume which can be maximally stored by a pm outside of its volume, therefore specifying the performance or strength of a pm. $(BH)_{max}$ is defined as the maximum rectangular area within the $B(H)$ hysteresis loop in the second quadrant as shown in Fig. 1b. The theoretical upper limit of $(BH)_{max}$ is given by the remanence according to $(BH)_{max}^{theo} = J_R^2/(4\ \mu_0)$. However, this limit can only be realized if the coercive field obeys the condition $\mu_0 H_C > 0.5\ J_R$ and if the $J(H)$ hysteresis loop is fully rectangular and reversible up to an inverse field of at least $0.5\ J_R$. Otherwise, $(BH)_{max}$ is limited by irreversible demagnetizing processes as sketched in Fig. 1b. Pms are employed for storage and transformation of energy (electric motors and generators, loudspeakers, microphones, ABS brake systems), for exerting a force on soft ferromagnetic objects or on mobile armatures (magnetic holding, separating, lifting and clamping) and for guidance of charged particles (hexapoles, control devices for electron beams, travelling wave tubes). The greater the $(BH)_{max}$ value of a pm material is the smaller may be the volume and therefore the weight of the magnet required for a given application task, under identical conditions. In fact, the trend for hard magnets is obviously directed towards smallest and most powerful magnets, particularly in technologies where miniaturization is required, enabling the invention of many new application fields and therefore a rapid growth in the worldwide market. Prominent examples for the need of compact pms are hard-disk drives and voice coil motors in computer data storage applications or magnetic resonance imaging systems in medicine. However, powerful pms are also very important in the scientific sector, e.g. for the construction of wigglers and undulators necessary for the generation of synchrotron radiation.

After this brief overview we will now present the recent progress made (in research) concerning pms. Generally, the characteristics of the hysteresis loop are determined by both the material (intrinsic magnetic properties) and the microstructure (extrinsic magnetic properties). Intrinsic magnetic properties are the Curie temperature T_C, the spontaneous polarization J_S, and the magnetocrystalline anisotropy constant K_1. In the case of a uniaxial crystal symmetry for a positive K_1, the spontaneous polarization orients parallel to the *c*-axis of the crystal and K_1 is a measure of the energy necessary for rotating the spontaneous polarization out of this easy axis. A large spontaneous polarization is a prerequisite for high J_R values, whereas a large magnetocrystalline anisotropy constant may result in large coercivities both ensuring high maximum energy products as described in Eq. 1. A high Curie temperature

finally enables the application of pms at high temperatures. Consequently, high-performance pms have to be based on high J_S-, K_1- and T_C-values ($J_S > 1.0\ T$, $K_1 > 10^6\ J/m^3$ and $T_C > 250\,°C$). On the other hand, the extrinsic magnetic properties can be tailored by the choice of the alloy composition from the phase diagram as well as by the processing routes. The most common preparation techniques for pms at present are sintering and melt-spinning leading to microcrystalline and nanocrystalline microstructures, respectively.

This review is organized as follows. In the next section, a survey of the most common hard magnetic materials and their fabrication is given. The correlation between the microstructure and the magnetic properties is then demonstrated for two types of RE–TM pms: (1) The ternary compound $RE_2Fe_{14}B$ (RE = Nd,Pr) which is currently regarded to be the highest performance pm material of all and which is well-suited for the newly developed polymer bonded magnets; and (2) the quintary compound $Sm_2(Co,Cu,Fe,Zr)_{17}$, which supplies the highest $(BH)_{max}$ values at elevated temperatures (beyond which $RE_2Fe_{14}B$ is no longer viable) therefore being well-suited for high-temperature applications. The correlation, which is rather complex, can be predicted quantitatively by using numerical micromagnetic simulations on the basis of the Finite Element technique. In the final section, general rules for the development of optimized pms are derived from such computational model calculations.

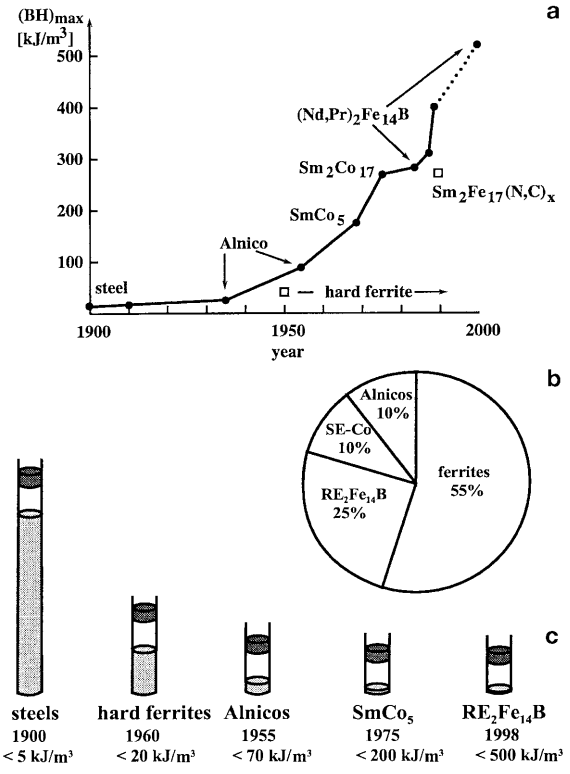

Fig. 2 **a** Progress in improving $(BH)_{max}$ of pm materials over the past century. **b** Total sales of the different permanent magnetic materials. **c** Schematic representation of the improvements of the weight-bearing capacity for a given piece of ferrite (*dark grey*) for the different types of materials (*light grey*) shown in Fig. 2a. The volume of the pm bodies has been chosen so that each represents the same total magnetic energy

Permanent magnet materials

During the twentieth century an extraordinary development in pm materials took place. Within the last 100 years the experimentally achieved maximum $(BH)_{max}$ values have increased exponentially from 2 kJ/m^3 to more than 400 kJ/m^3 (i.e. a doubling every 12 years; see Fig. 2a and Table 1). In Fig. 2c an alternative manner of representation has been used to illustrate the effect of this progress. The figure shows the drastic decrease by several hundred-fold in the volume necessary for the various kinds of hard magnetic materials to provide the same weight-bearing capacity or performance, respectively. In the first 40 years of the twentieth century the pms market was dominated by C-, W-, and Co-steels (with C, W and Co providing pinning sites): the classical horseshoe magnets. These magnets were superseded in the 1940s by the AlNiCo magnets (Kneller 1962; McCurrie 1982; Buschow 1997) which owe their properties to the shape anisotropy of small elongated ferromagnetic FeCo particles precipitated in a weakly magnetic AlNi matrix. The next step forward was in the 1950s with the development of the hexagonal hard ferrites of the type $(Ba/Sr)Fe_{12}O_{19}$ (ceramic magnets) (Kojima 1982; Kools 1992; Buschow 1997), whose low crystal symmetry leads to a high magnetocrystalline anisotropy (see Table 1). The decisive breakthrough, however, came at the end of the 1960s with the intermetallic rare earth (RE) transition metal (TM) compounds on the basis of Sm–Co ($SmCo_5$, $Sm_2(Co,Cu,Fe,Zr)_{17}$) (Strnat et al. 1967; Kronmüller 1978; Kumar 1988; Strnat 1988; Buschow 1997), Sm–Fe ($Sm_2Fe_{17}N_3$, $Sm_2Fe_{15}Ga_2C_2$) (Coey and Sun 1990; Shen et al. 1993; Buschow 1997) and RE-Fe-B ($Nd_2Fe_{14}B$, $Pr_2Fe_{14}B$) (Croat et al. 1984; Hadjipanayis et al. 1984; Sagawa et al. 1984; Buschow 1988, 1997). They derive

Table 1 Intrinsic magnetic properties (T_C: Curie temperature, J_S: spontaneous polarization, K_1: crystal anisotropy constant) and maximum $(BH)_{max}$ values of the different pm materials of the twentieth century (Buschow 1997)

Material	K_1 [MJ/m^3]	J_S [T]	T_C [°C]	$(BH)_{max}$ [kJ/m^3]
Steel	0.046	2.15	770	2
AlNiCo	0.04	1.20	860	45
Ba-ferrite	0.3	0.47	450	23
$SmCo_5$	17	1.06	727	180
$SmCo_{17}$	3.9	1.25	916	260
$Nd_2Fe_{14}B$	4.3	1.61	312	450
$Pr_2Fe_{14}B$	5.6	1.56	292	–
$Sm_2Fe_{17}N_3$	8.9	1.53	477	250
$Sm_2Fe_{15}Ga_2C_2$	5.2	1.02	362	–

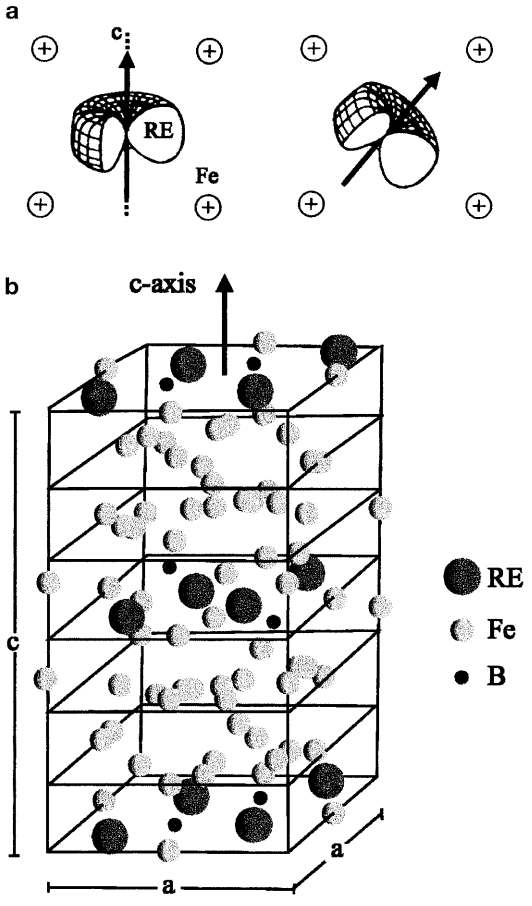

Fig. 3 **a** Reason for the high magnetocrystalline anisotropy (*left*: ground state $H=0$, *right*: rotation under a magnetic field). **b** Tetragonal crystal structure of the ternary $RE_2Fe_{14}B$ (RE = Nd,Pr) compound

their exceptional magnetic properties from the favourable combination of the high saturation polarization and Curie temperature of the 3d TM with the extremely high crystal anisotropy constant provided by the 4f RE metals (see Table 1). Thence, the high crystal anisotropy arises as follows: the aspheric electron charge distribution of the localized 4f electrons of the RE atoms is coupled with the magnetic moment according to the spin-orbit interaction (Hund's rules) and interacts with the neighbouring TM atoms. For $H_{ext}=0$ (ground state) the alignment of the magnetic moment into the direction of the *c*-axis is energetically most favoured. This is illustrated in Fig. 3a. As an example, Fig. 3b displays the unit cell of $RE_2Fe_{14}B$ (RE = Nd,Pr). The lattice symmetry is tetragonal (lattice constants $a=8.8$Å, $c=12.2$Å) and each unit cell consists of 68 atoms, whose arrangement is such that layers of Fe atoms alternate periodically with layers containing rare earth metal atoms.

Certainly, it is not reasonable to choose the material with the highest $(BH)_{max}$ value for any given application. Rather, the wide field of applications calls for an extensive range of pm materials with many different characteristics of the hysteresis loop, sizes and shapes, whereby in the majority of cases economical considerations play the most important role. Therefore, it is not surprising that hard ferrites still account for half the value of all pms produced worldwide. Their great popularity is due to the low cost of their raw materials, their chemical stability and high electrical resistance. The other half of the market is mostly for RE magnets with their maximum energy products up to 15 times larger than for ferrites. Hereby, magnets based on Sm and Co ($SmCo_5$, $Sm_2(Co,Cu,Fe,Zr)_{17}$) still supply the highest coercive fields ($\mu_0 H_C > 3.5\ T$ at room temperature) as well as Curie temperatures ($T_C > 1000$ K) attainable today. Another feature is their low temperature coefficient of coercivity $d(\mu_0 H_C)/dT$ at elevated temperatures which have been improved drastically in the last few years and which makes them well-suited for high-temperature applications. On the other hand, since magnets based on $RE_2Fe_{14}B$ (RE = Nd,Pr) reveal a very large spontaneous polarization of 1.6 *T*, they are unsurpassed with regard to their maximum energy products, significantly exceeding all previous values [$(BH)_{max} > 400$ kJ/m^3 is the record value held for well-oriented sintered magnets at present] and their comparatively cheap constituent materials compared with Sm–Co type magnets. In addition, the ternary RE–Fe–B phase diagram enables a proper design of magnets with quite specific properties of the hysteresis loop. The production of AlNiCo magnets is rather low but still substantial due to their outstanding temperature behaviour and high corrosion resistance. Fig. 2b summarizes how the total sale is broken down today into the four categories. The total world production of pms is in the order of 250,000 tons per year ($\approx 4 \cdot 10^9$ US dollar) with an annual growth rate between 10 and 20%. For the interstitial intermetallics, $Sm_2Fe_{17}N_3$ and $Sm_2Fe_{15}Ga_2C_2$, which were developed in the early 1990s, the step into large-scale production is still missing.

There are two basic mechanisms responsible for producing large coercive fields, i.e., for the so-called magnetic hardening, namely, the reversal of the magnetization by nucleation of reversed domains (nucleation mechanism) and the reversal of the magnetization by displacement of pinned domain walls (pinning mechanism). The first of these processes is connected with the existence of small isolated hard magnetic particles or grains which consist of one single domain. The second is associated with magnetic inhomogeneities which are present in the grains and which act as pinning centres for domain wall motion. The most effective pinning centres are planar defects, because then the whole wall area is involved. Further inhomogeneities which may occur are precipitates, point defects, dislocations and antiphases. The coercive field of both nucleation as well as pinning hardened materials is well-described by the universal relation (Kronmüller 1987, 1991; Sagawa and Hirosawa 1987)

$$\mu_0 H_C = \mu_0 \frac{2K_1}{J_S} \alpha - N_{eff} J_S \quad (1)$$

Here, the first and second terms represent modified magnetocrystalline and demagnetizing fields, where α and N_{eff} correspond to microstructural parameters which describe the effect of the microstructure on these effective fields and which in turn may depend on the intrinsic material parameters. For ensembles of polyhedral grains, N_{eff} is usually found to be positive, whereas for elongated needle-like particles, N_{eff} is negative. The microstructure of a solid is understood by all deviations from the ideal crystal structure. In the case of nucleation hardened magnets, α results from regions where the magnetocrystalline anisotropy is reduced (α_K), e.g. from grain boundaries, as well as from misaligned grains (α_ψ) and can be written as $\alpha = \alpha_K \alpha_\psi$. For pinning hardened magnets, α describes the strength of the domain wall pinning centres and shows values up to approximately 0.3 (Kronmüller et al. 1988). The microstructural parameters, and therefore the microstructure, are the reason for Brown's paradox (Brown 1945), i.e. the experimentally realized $\mu_0 H_C$ values are only 20–30% of the theoretically achievable values ($\alpha = 1$, $N_{eff} = 0$) which are given by the so-called ideal nucleation field $\mu_0 H_N$ of a spherical single-domain particle whose magnetization is reversed by an irreversible homogeneous rotation process ($\mu_0 H_N = \mu_0 H_{C,max}^{theo} = 2\,\mu_0 K_1 / J_S$) (Brown 1945). It should be noticed that Eq. 2 also reflects the importance of large K_1 values for obtaining large coercivities. Typical nucleation-hardened magnets are magnets of Ba-ferrite, $SmCo_5$ and $(Nd,Pr)_2Fe_{14}B$. Domain-wall pinning is realized in classical steel-based magnets and in $Sm_2(Co,Cu,Fe,Zr)_{17}$ type magnets. Al-NiCo magnets are based on the so-called form effect, i.e. to the second term in Eq. 2 with a negative N_{eff}.

Modern pms are based on ensembles of small hard magnetic grains. For manufacturing, two principial processing routes have been devised – sintering and melt-spinning. Whereas the former leads to anisotropic microcrystalline magnets (particle size 1–20 μm, multidomain particles), with the latter process, isotropic magnets (particle size 10–200 nm, single-domain particles) can be obtained (isotropic means that the easy axes of the hard magnetic grains are isotropically distributed). In both cases, master alloys of the nominal composition have first to be prepared by induction melting or arc melting from the constituent elements. For the sintering process the prealloy is then milled into a powder of small single crystallites typically between 5–30 μm in size. The powder is pressed under an applied magnetic field so that the easy axes of the crystallites are more or less orientated along the field direction and sintered at 1000–1100 °C. The degree of this texture and hence the quality of the magnet depends mainly on the magnetic field strength, the particle size and the shape of the grains. Sintered magnets have to be after-treated by sawing or grinding. For the melt-spinning process the prealloy is melted inductively in a quartz nozzle and the melt is ejected on a rotating copper wheel with surface velocities ranging from 10 m/s to 40 m/s where it solidifies at a cooling rate of up to 10^6 K/s and is thrown off the wheel in the form of ribbon flakes (typical thickness 20–40 μm.). Depending on the cooling rate and therefore on the wheel velocity, ejection conditions and melting temperature, a fine-grained nanostructure can be obtained either directly or by overquenching the ingots into (partly) amorphous ribbons followed by a subsequent heat treatment. The nanocrystalline ribbons can be powderized and bonded with epoxy to form isotropic polymer bonded magnets. Other methods used for processing nanocrystalline hard magnetic materials are mechanical alloying and the hydrogenation, disproportionation, desorption and recombination (HDDR) process (Harris1996; Buschow 1997). Up until now, sintering has been the commercially most important process. However, melt-spinning combined with polymer bonding is gaining in importance, especially in the case of $RE_2Fe_{14}B$ (RE = Nd,Pr).

Microstructure and magnetic properties

Microcrystalline permanent magnets

RE-Fe-B

Sintered magnets based on $RE_2Fe_{14}B$ (RE = Nd,Pr) involve starting alloys that are highly enriched in RE. During the sintering process a paramagnetic RE-rich intergranular phase develops between the μm-scaled and highly oriented hard magnetic $RE_2Fe_{14}B$ grains, yielding a more or less magnetic isolation of the grains which promotes large coercivities. Fig. 4a reveals the domain structure of a thermally demagnetized NdFeB-oriented sintered magnet done with the (longitudinal) Kerr microscopy (Chen and Kronmüller 1990). The average grain size is about 20 μm and most of the grains exhibit a multidomain state well-oriented along the texture axis. The decoupling of the grains and therefore the coercivity can be further improved by mixing small amounts of Ga and Nb (Herbst 1991; Fidler 1992). The low-melting refractory metal Ga greatly improves the viscosity of the intergranular phase in the liquid state, which enables a more perfect encapsulating of the grains. The high-melting refractory metal Nb prevents grain growth by forming precipitates and high-melting NbFe borides. The effect of Ga and Nb on the magnetic properties can be seen from Fig. 4b where the hysteresis loops of the two aligned sintered magnets $Nd_{15}Fe_{77}B_8$ and $Nd_{18}Fe_{74}B_6Ga_1Nb_1$ are compared with each other (Kronmüller et al. 1996). Obviously, H_C increases significantly with the additives Ga and Nb. Furthermore, the high rectangularity of the hysteresis loops is an important feature of aligned sintered pms. Sintered REFeB based magnets are typical nucleation hardened magnets revealing large values for the micro-

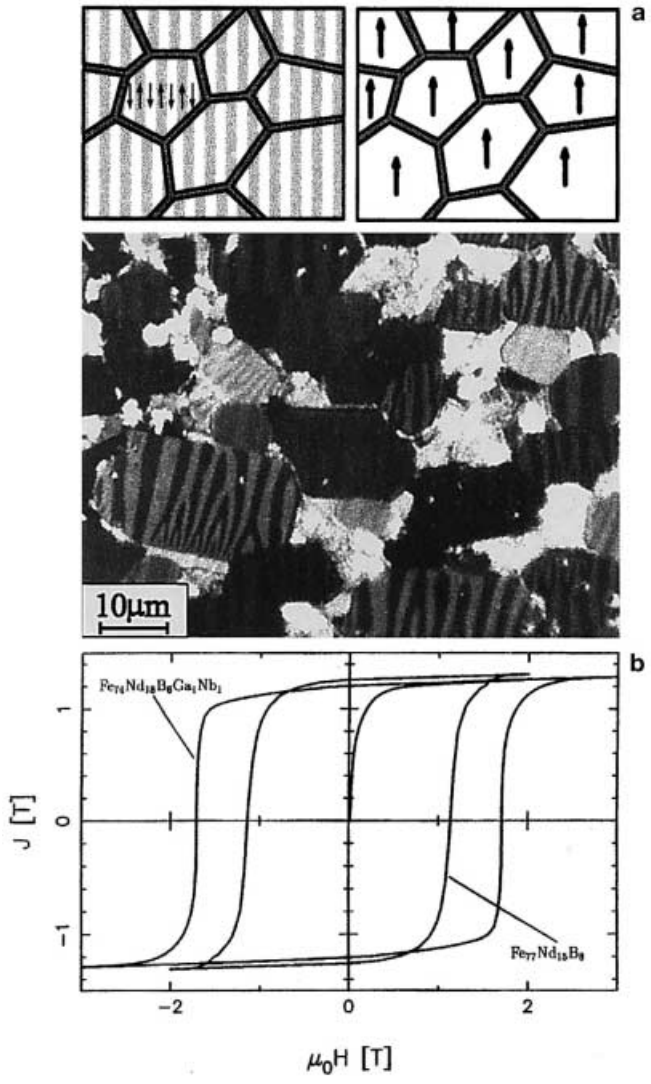

Fig. 4 **a** Schematic microstructures of a microcrystalline anisotropic $RE_2Fe_{14}B$ magnet in the demagnetized state (*left*) and the state after saturation (*right*) and Kerr micrograph of a thermally demagnetized NdFeB oriented sintered magnet whereby the *stripes* represent domains. After saturation there is one single domain left in the grains. **b** Hysteresis loops of different NdFeB based sintered magnets

structural parameters of $\alpha_K = 0.9$ and $N_{eff} = 2.0$ (Kou et al. 1994). These large values can be attributed to the comparatively perfect grain surfaces and the sharp edges and corners of the grains formed during the sintering process.

$Sm_2(Co,Cu,Fe,Zr)_{17}$

The typical pinning hardened $Sm_2(Co,Cu,Fe,Zr)_{17}$ based sintered magnets show α values in the order of 0.3 (von Zeppelin 1999). Their hard magnetic properties are obtained after the following sequence of heat treatments (see e.g. Kronmüller et al. 1984; Buschow 1997). After homogenizing at $T_h = 1100$–$1200\,°C$ for $T_h \approx 30$ min and quenching to room temperature the specimens are isothermally aged at $T_a \approx 850\,°C$ for $t_a = 10$–25 h, succeeded by a slow cooling (rate of 0.5–1 °C/min) down to 400 °C. The final step is the quenching to room temperature. During this annealing procedure a complicated microstructure (see Fig. 5a) develops. One finds a rhombic structure parallel to the *c*-axis. The cells (**A**) are of about 100 nm in size and

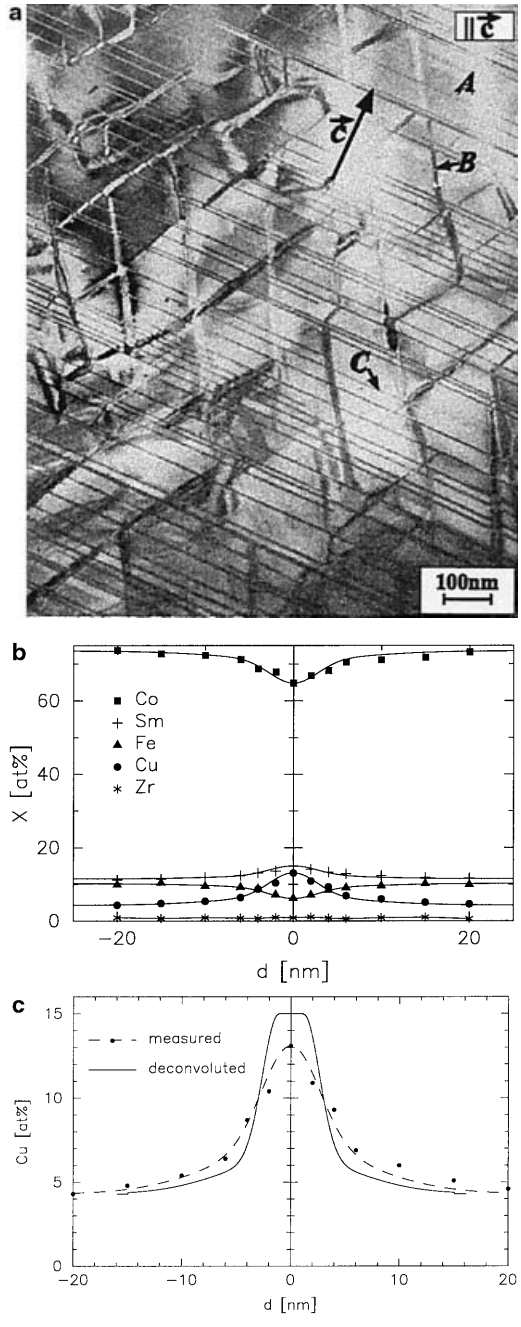

Fig. 5 **a** TEM micrograph of a $Sm_2(Co,Cu,Fe,Zr)_{17}$ based sintered magnet observed parallel to the *c*-axis. **b** EDX investigation of the distribution of the elements in the vicinity of a 2:17/1:5 phase boundary (X = Sm,Co,Cu,Fe,Zr). **c** Measured Cu profile in comparison with the deconvoluted one calculated assuming a circular spot of 1 nm and a Gaussian broadening of 7 nm

consist of a Fe-rich but Cu-/Zr-poor 2:17 matrix phase. They are more or less separated by a Cu-rich, Fe-/Zr-poor boundary phase (**B**) of about 5–10 nm which is of 1:5 stoichiometry. In the basal plane this network is hexagonal, indicating that the boundary phase lies on pyramidal surfaces. Additionally, a Zr-rich platelet phase (C) of 2–4 nm in width, which is orientated perpendicularly to the *c*-axis, is superimposed on the cellular microstructure. This so-called lamellar *Z* phase extends through quite a lot of cells and cell boundaries. As an example, Fig. 5b shows a scan of the elements standardized to the Co content from one 2:17 cell over a 1:5 cell boundary into another cell of a $Sm_2(Co,Cu,Fe,Zr)_{17}$ based magnet measured by means of energy dispersive X-ray analyses (EDX) (Goll et al. 2000b). It should be noted that such profiles are a convolution of the real chemical profile and the resolution function of the probe. For example, Fig. 5c shows the real chemical profile of the measured Cu profile obtained by deconvolution (Goll et al. 2000b). The thin prismatic 1:5 precipitates encapsulating the 2:17 cells provide pinning centres for domain wall motion (Kronmüller et al. 1984). In general, a pinning force arises when a domain wall is driven from a region with low wall energy into one with larger wall energy. Depending on the Cu content the cell walls correspond to regions of higher (in the case of low Cu content) or lower (in the case of high Cu content) anisotropy constants compared with the cells. Therefore, domain walls which are moving through a cell are repelled or trapped, respectively, by the cell wall and are pushed in both cases over the big potential barrier when the applied field reaches the coercive field. The largest coercive field achieved in such magnets is $\mu_0 H_C \approx 3.5\ T$. $Sm_2(Co,Cu,Fe,Zr)_{17}$ based magnets are characterized by an extremely good temperature stability up to high temperatures, which can be influenced by the chemical composition and the parameters of the heat treatment (Chen et al. 1998; Liu et al. 1998).

Clearly, oriented sintered magnets show the highest remanences and $(BH)_{max}$ values of all at least along their texture axis. Furthermore, the degree of their texture can be varied during the manufacturing process. However, the major drawbacks of sintered magnets are that they have to be after-treated by sawing or grinding and that they are very hard and brittle. Therefore, their shape formation is limited to a few simple geometries. Moreover, due to their high RE content and the sintering technique itself, they are relatively expensive. Nevertheless, if highest-performance pms are needed, well-oriented sintered magnets have to be used.

Nanocrystalline permanent magnets

Nanocrystalline hard magnets on the basis of $RE_2Fe_{14}B$ (RE = Nd,Pr) are well-suited for tailoring magnets with definite properties of the hysteresis loop. Thus, one takes the advantage of the fact that small deviations

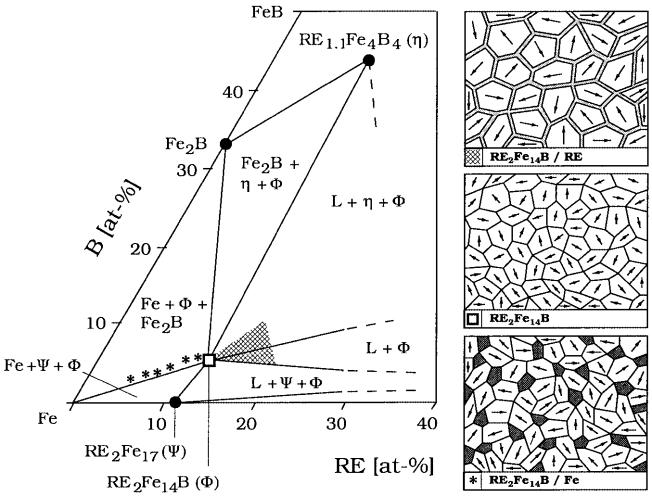

Fig. 6 Ternary phase diagram RE-Fe-B (RE = Nd,Pr) at $T = 1000\,°C$ and schematic microstructures for the demagnetized state of the three types of nc pms characteristic for the three (composition) ranges indicated

from the stoichiometry and small amounts of certain additives may result in a dramatic change in the magnetic properties. Based on the phase diagram, three types of nanocrystalline pms with different microstructures have been developed by means of the melt-spinning method – stoichiometric magnets, magnets with RE-excess (decoupled magnets) and magnets with overstoichiometric Fe (composite magnets). Fig. 6 presents the ternary RE-Fe-B phase diagram (Schneider et al. 1986; Henig and Grieb 1991) – an isothermal section at 1000 °C of the Fe-rich corner – and the schematic microstructures of the three prototypes characteristic for the three marked ranges. The corresponding HRTEM micrographs (Zern 1995; Kronmüller et al. 1999) and room temperature hysteresis loops (Goll et al. 1998) are shown in Figs. 7 and 8, respectively.

Decoupled magnets (high-coercive magnets)

For nanocrystalline decoupled magnets or high-coercive magnets, the composition has to be taken from the same regions which come into question for REFeB sintered magnets – namely, from the 'conventional' regions $L + \Phi$ and $L + \eta$ where in addition to the hard magnetic Φ-phase the RE-rich L-phase (which is liquid at 1000 °C) and η-phase ($RE_{1.1}Fe_4B_4$) occur. Accordingly, the resulting microstructure obtained by melt-spinning qualitatively agrees with the situation in sintered pms where single crystallites of the hard magnetic phase are more or less magnetically decoupled by a paramagnetic RE-rich boundary phase. (There still exist some long-range dipolar interactions between the hard magnetic grains which, however, play only a minor role.) However, the scale is about a factor of 100 smaller now and the easy axes of the nanoscaled grains are isotropically distributed. The high resolution TEM

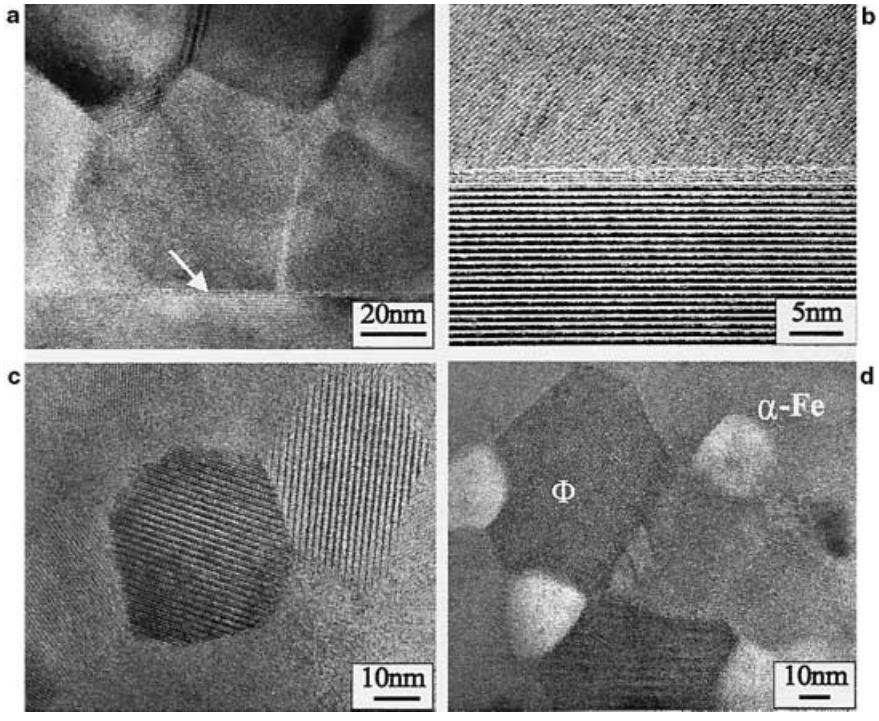

Fig. 7 High-resolution TEM micrographs of the three different types of nanocrystalline $RE_2Fe_{14}B$ based magnets (RE = Nd,Pr): **a** exchange decoupled magnet with overstoichiometric RE, **b** the same as in (**a**) but with a higher magnification to illustrate the RE-rich intergranular phase, **c** exchange-coupled single-phase magnet of the stoichiometric composition $RE_2Fe_{14}B$ and **d** exchange-coupled composite magnet with overstoichiometric Fe (15%)

(HRTEM) micrographs in Figs. 7a and b present the intergranular film with a thickness of about 2 nm as a bright region between the nanoscaled grains. This reveals a disordered structure where three quasi-planes show a corrugated amorphous structure. The dark fringes in the grains with a distance of 1.2 nm correspond to the extension of the $RE_2Fe_{14}B$ unit cell in the direction of the tetragonal *c*-axis. The energy dispersive *X*-ray technique (EDX) (Zern et al. 1998) clearly shows the enrichment of the rare earth metal within the intergranular phase. It should be noted that the grain size ranges from 50 to 200 nm, which guarantees that mainly single-domain particles exist. The typical hysteresis loop of such a pm is represented in Fig. 8b. This shows a very large coercivity of 2.5 *T* and a remanence of 0.78 *T*. This hysteresis loop can be better understood with Fig. 9a. In the saturated state the polarization is oriented into the direction of the applied field, whereas in the remanent state the polarization has rotated back into the local easy direction of each grain due to the crystal anisotropy. Since the easy directions are isotropically distributed (in the upper half-sphere) this results

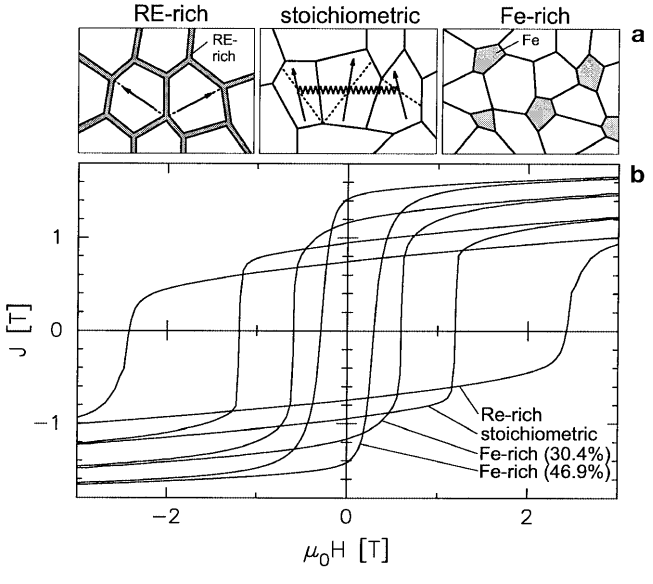

Fig. 8 The three different types of nanocrystalline $RE_2Fe_{14}B$ based magnets (RE = Nd,Pr) – $RE_2Fe_{14}B$/RE (highest coercivity), $RE_2Fe_{14}B$ (high coercivity, high remanence) and $RE_2Fe_{14}B$/Fe (highest remanence): **a** (schematic) microstructures for the remanent state and **b** room temperature hysteresis loops

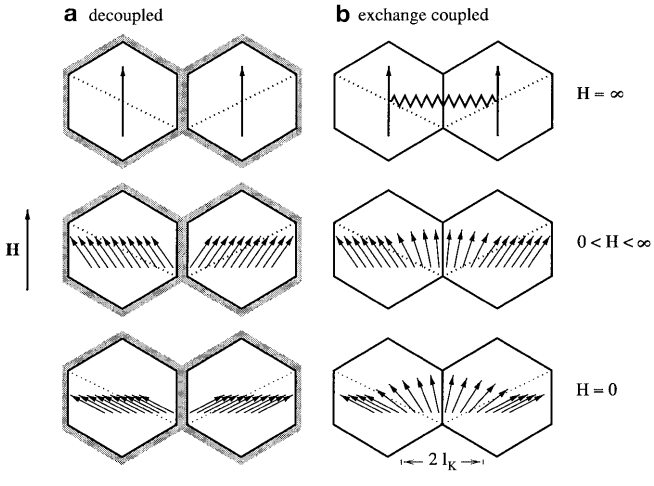

Fig. 9 Comparison of the orientation of the (spontaneous) polarization in the saturated state $H = \infty$, in the state $0 < H < \infty$ and in the remanent state $H = 0$ for an exchange decoupled magnet (**a**) and an exchange coupled magnet (**b**)

in a remanence of maximum one-half of the spontaneous polarization (Stoner and Wohlfarth 1948) ($J_R \leq 0.5\, J_S$, $J_S = 1.6\ T$). On the other hand, the reason for the high coercivity values is that each grain behaves like an elementary pm (i.e. for demagnetizing, the reversed applied field first has to overcome the crystal anisotropy). As in the case of sintered magnets the decoupling, and therefore the coercivity, can be improved by adding small amounts of Ga and Nb and/or by subsequent annealing treatments (e.g. 700 °C/15 min).

Stoichiometric magnets (high-remanent / high-coercive single-phase magnets)

Nanocrystalline stoichiometric magnets are received for the stoichiometric composition $RE_2Fe_{14}B$ (Manaf et al. 1991; Bauer et al. 1996; Goll et al. 1998). In such (high-remanent/high-coercive) single-phase magnets the hard magnetic grains are directly connected without any intergranular phase and therefore they are magnetically coupled by exchange interactions. The HRTEM micrograph in Fig. 7c indeed shows such a single-phase nanostructure for the melt-spun stoichiometric alloy $RE_2Fe_{14}B$ with an average grain size of 20 nm. The addition of small amounts of Zr (Goll and Kronmüller 1998) and Nb (Hadjipanayis 1999) contributes to a further refinement of the hard magnetic grain structure. In the case of stoichiometric magnets, a significantly enhanced remanence and a slightly reduced coercivity – both quantities are in the order of 1 T now (see Fig. 8b) – are observed as a consequence of the exchange coupling between the grains. The effects of the exchange interaction on the hysteresis loop can be understood with the aid of Fig. 9b. In the remanent state the polarization cannot align parallel to the isotropically easy directions of the grains, as in the case of decoupled magnets, since the exchange interaction counteracts this process by trying to align the polarization of neighbouring grains parallel to each other. This is symbolized in Fig. 8a by a spring. However, as the exchange interaction is a very short-range interaction – a measure for its range is the so-called Bloch wall width $\delta_B = \pi\sqrt{A/K_1}$ (A: exchange constant) which is in the order of 4 nm for $RE_2Fe_{14}B$ – its influence is largest at the grain boundary and disappears inside the grain. Thus, the polarization direction underlies a smooth transition from the easy axis of one grain to the easy axis of another grain. Or in other words, within the wall width δ_B a magnetic texture is induced with the texture axis parallel to the original saturation polarization (i.e. the direction of the initially applied field). Since only this exchange coupled volume fraction can bring about the remanence enhancement, the grain size should be smaller than 50 nm (Fischer et al. 1995) in order to notice the remanence enhancing effect macroscopically. Hence, with diminishing grain sizes J_R increases. The exchange coupling between the grains is also the reason for the smaller coercivity values compared to decoupled magnets. As part of the moments is already rotated out of the easy axis, for demagnetization a smaller reversed applied field is sufficient. Therefore, with diminishing grain sizes H_C decreases.

Composite magnets (high-remanent two-phase magnets)

If the alloy composition is chosen near to the two-phase line Fe-Φ on the left region bordering the stoichiometric Φ phase (Fig. 6) a second type of exchange-coupled magnets, the so-called composite magnets (Kneller and Hawig 1991; Manaf et al. 1993; Gong et al. 1994; Withanawasam et al. 1995; Bauer et al. 1996; Goll et al. 1998), can be obtained, showing a further significant increase of the remanence-enhancing effect, accompanied by a further reduction of the coercivity as can be seen from Fig. 8b. In such high-remanent two-phase magnets nanocrystalline soft magnetic α-Fe grains arise in addition to the hard magnetic $RE_2Fe_{14}B$ grains from the melt-spinning process as a consequence of the over-stoichiometric α-Fe. Thus, the remanence enhancement is due to the exchange coupling among the grains but also to the very large spontaneous polarization of the α-Fe grains ($J_S = 2.15\ T$) which significantly intensifies the magnetic texturing effect. Since the crystal anisotropy of a soft magnet in general is very small, the polarization of α-Fe is pinned by the hard magnetic phase so that the soft magnetic properties disappear macroscopically and the sample behaves magnetically single-phase (so-called exchange hardening). However, to obtain excellent hard magnetic properties in such composite magnets, it is imperative that the soft magnetic α-Fe grains are completely exchange-coupled with the hard magnetic grains. Therefore, their size may not exceed a certain limit which is in the order of the Bloch wall width δ_B of the hard magnetic phase (Kronmüller et al. 1996). Otherwise, the hysteresis loop would show a two-step demagnetization behaviour with drastically deteriorated hard magnetic properties. For this reason, sintered magnets with their µm-scaled grains cannot be realized with compositions in the Fe-rich region of the phase diagram. Fig. 7d reveals a typical HRTEM micrograph of a nanocrystalline exchange coupled composite magnet showing small soft magnetic α-Fe grains (≈ 15 nm) which contact without any intergranular phase the hard magnetic $RE_2Fe_{14}B$ grains (20–30 nm). That the smaller grains represent the α-Fe grains and the larger ones $RE_2Fe_{14}B$ could be confirmed by energy dispersive X-ray microanalysis (Manaf et al. 1993) and by determining the lattice spacings using the HRTEM technique (Zern et al. 1998).

Fig. 10a summarizes the dependence of J_R and $\mu_0 H_C$ as a function of the iron content of melt-spun $Pr_2Fe_{14}B$/α-Fe magnets at room temperature (Goll et al. 1998). In addition, the behaviour of the maximum energy product $(BH)_{max}$ is presented. With an increasing

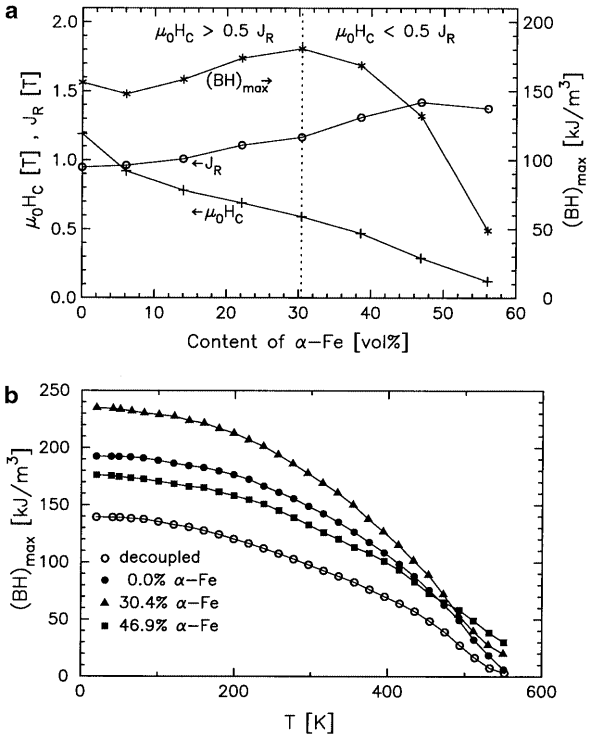

Fig. 10 **a** $\mu_0 H_C$, J_R and $(BH)_{max}$ as a function of the α-Fe content for PrFeB composite pms at room temperature. **b** Temperature dependence of the maximum energy product of $Pr_2Fe_{14}B/\alpha$-Fe composite magnets in comparison with the decoupled magnet $Pr_{15}Fe_{78}B_7$

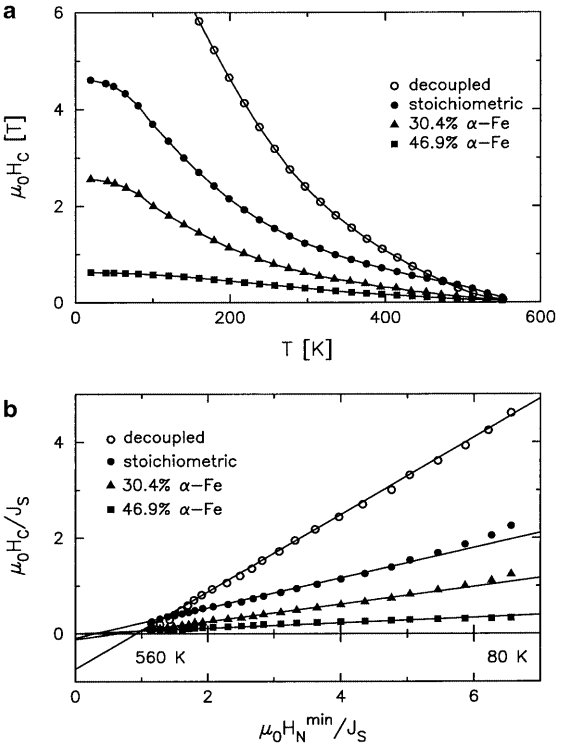

Fig. 11 **a** Temperature dependence of the coercivity of $Pr_2Fe_{14}B/\alpha$-Fe composite magnets in comparison with the decoupled magnet $Pr_{15}Fe_{78}B_7$. **b** $\mu_0 H_C/J_S$ versus $\mu_0 H_N^{min}/J_S$ plot to determine the microstructural parameters of the different PrFeB magnets of Fig. 11a

amount of α-Fe the remanence becomes larger up to a maximum value of 1.42 T in $Pr_6Fe_{90}B_4$ containing 46.9 vol% α-Fe – a value which is quite comparable with well-oriented sintered magnets. This, however, comes at the expense of the coercivity, which is continually reduced with increasing α-Fe concentration. On the other hand, the maximum energy product shows a maximum value of $(BH)_{max} = 180.7$ kJ/m^3 for 30.4 vol% α-Fe which means an increase by a factor of nearly two as compared with a conventional nanocrystalline decoupled magnet of composition $Pr_{15}Fe_{78}B_7$ ($(BH)_{max} = 99.7$ kJ/m^3). As at low α-Fe concentrations (<30 vol%) the coercive field obeys the condition $\mu_0 H_C > 0.5\ J_R$, $(BH)_{max}$ sensitively depends on the remanence according to the theoretical upper limit valid for isotropic samples (see Eq. 1). This gives the reason for the enhancement of $(BH)_{max}$ with increasing remanence. However, as at high α-Fe concentrations (>30 vol%) the coercive field becomes smaller than one half of the remanence, $(BH)_{max}$ is restricted by irreversible demagnetization processes leading to a drastic decrease of $(BH)_{max}$. This behaviour of the magnetic properties discussed here in the case of room temperature as a function of the composition is well-developed in the whole ferromagnetic temperature range ($0 < T < T_C$) as can be seen from Fig. 10b for the maximum energy product and from Fig. 11a for the coercivity. If the content of α-Fe increases, this improves the thermal stability of the coercive field and also of the remanence (Goll and Kronmüller 1998). The temperature dependence of the coercive field can be described quantitatively within the framework of the nucleation model by using a modified form of Eq. 2 (Bauer et al. 1996):

$$\mu_0 H_C(T) = \alpha_K \alpha_{ex} \mu_0 H_N^{min}(T) - N_{eff} J_S(T) \qquad (2)$$

with the microstructural parameter α_{ex} which takes into account the effect of the exchange coupling between the hard and soft magnetic grains ($\alpha_{ex} = 1$ for decoupled magnets) and with the minimum nucleation field $\mu_0 H_N^{min} = 2\,\mu_0 K_1\,\alpha_\psi / J_S$. $\mu_0 H_N^{min}$ denotes the value for the nucleation field of the most unfavourably aligned grains which are responsible for the demagnetization of the whole sample (the smallest nucleation fields have particles with a misalignment of about 45°). $H_N^{min}(T)$ is determined by the intrinsic material parameters $K_1(T)$, $K_2(T)$ and $J_S(T)$ which are well-known from measurements made using single crystals (Martinek and Kronmüller 1990). If the nucleation model is valid, plotting the experimental data $\mu_0 H_C/J_S$ versus the theoretical values $\mu_0 H_N^{min}/J_S$ should lead to a straight line with slope $\alpha_K \alpha_{ex}$ and ordinate intersection ($-N_{eff}$) in the case of temperature independent microstructural parameters. This evaluation is shown in Fig. 11b for the three different types of nanocrystalline PrFeB magnets (Goll et al. 1998). In fact, an approximately linear relation-

Table 2 Microstructural parameters depending on the α-Fe content

Nominal composition	$\alpha_K \alpha_{ex}$	N_{eff}
$Pr_{15}Fe_{87}B_7$ (decoupled)	0.80	0.74
$Pr_{12}Fe_{82}B_6$ (stoichiometric)	0.32	0.09
$Pr_8Fe_{87}B_5$ (30.4% α-Fe)	0.18	0.12
$Pr_6Fe_{90}B_4$ (46.9% α-Fe)	0.06	0.00

ship is found for all compositions within the whole ferromagnetic temperature range. The results for $\alpha_K \alpha_{ex}$ and N_{eff} calculated from the balance straight lines are summarized in Table 2. Accordingly, the exchange coupled magnets have a significantly smaller slope and axis intersection of the straight line than the decoupled magnet. The decrease in $\alpha_K \alpha_{ex}$ from 0.8 for the decoupled magnet to 0.06 for an α-Fe content 46.9% reflects the decrease in the coercivity and can be attributed to the exchange coupling between the grains leading to a collective reversal behaviour and therefore to a reduction in the (effective) anisotropy constant. On the other hand, the decrease in N_{eff} is caused by a more spherical grain shape and by a reduction of local stray fields at the edges and corners of the grains due to the smoothing effect of the exchange interaction at the grain boundaries. As the parameter α_K is well-known from the decoupled magnet ($\alpha_K \approx 0.8$ (Seeger et al. 1994)) the microstructural parameters α_K and α_{ex} can be separated in the case of exchange-coupled magnets.

Nanocrystalline exchange coupled RE-Fe-B based magnets are optimally suited for the industrial fabrication of polymer-bonded magnets due to their high $(BH)_{max}$ values and their low RE content compared with conventional magnets, which reduces the cost of the raw materials and improves the corrosion resistance. Bonded magnets are made by powderizing the ribbons (powder particles < 50 μm), mixing the powder with a polymer, followed by compression-moulding or injection-moulding, i.e. magnetic powder particles are embedded in a non-magnetic matrix. In the case of bonded magnets, any final shape can be prepared easily without expensive after-treatment like sawing or grinding. Such magnets are characterized by low brittleness and low electric conductivity, and furthermore by their isotropy which is needed in multipole applications since the oriented sintered magnets can only be magnetized along the texture axis. The major drawback to bonded magnets is the reduction in their magnetic properties relative to their fully dense counterpart. This reduction can be estimated with the so-called filling factor, f, which reflects the volume fraction of the magnetic powder in the bonded magnet according to $(BH)_{max}^{bond} = f^2 (BH)_{max} \approx 50\% (BH)_{max}$. To maximize the filling density the objective is clearly to make the powder particles as small and round as possible and to minimize the volume fraction of the polymer while still maintaining adequate flow characteristics for moulding the compound and sufficient particle bonding for good

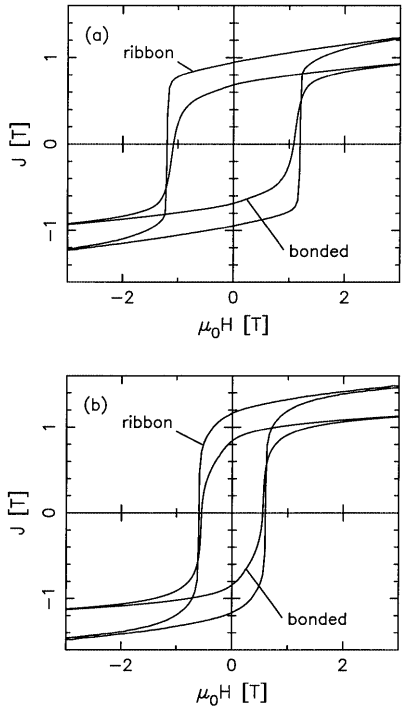

Fig. 12 Room temperature hysteresis loops of **a**, a polymer bonded $Pr_2Fe_{14}B$ magnet and **b**, a polymer bonded $Pr_2Fe_{14}B/\alpha$-Fe composite magnet, in comparison with the corresponding ribbon material

mechanical properties. Nevertheless, for many applications this drawback is far outweighed by the advantages mentioned above. In Fig. 12a and b the room temperature hysteresis loops of polymer bonded magnets of powderized nanocrystalline $Pr_2Fe_{14}B$ (stoichiometric) and $Pr_2Fe_{14}B/30.4\%\,\alpha$-Fe ribbons (density 6.0 g/cm^3) can be seen in comparison with loops of the corresponding ribbon material. The best $(BH)_{max}$ values obtained up to now at room temperature for this class of magnets are in the order of 90 kJ/m^3 (D. Goll et al. 2000a). When introducing preferred orientation by hot pressing the ribbons followed by die upsetting, the powder received is anisotropic. It can be processed into aligned bonded magnets providing higher maximum energy products (Buschow 1997). Finally, it should be noted that we have also succeeded in receiving the typical $Sm_2(Co,Cu,Fe,Zr)_{17}$ microstructure in melt-spun samples (Goll et al. 2000b), which makes them well-suited for (ceramic) bonding in the future.

Computer simulations

With numerical micromagnetic simulations the correlation between the microstructure and the magnetic properties of nanocrystalline exchange coupled magnets can be treated quantitatively for realistic microstructures. Thus, the magnetic state of an ensemble of

grains is obtained from the minimization of the magnetic free enthalpy ϕ_{tot}

$$\delta G = \delta \int \phi_{tot} dV = \delta \int (\phi_A + \phi_K + \phi_S + \phi_H) dV = 0 \quad (3)$$

whereby ϕ_{tot} is composed of four contributions: the exchange energy $\phi_A = A(\nabla\varphi)^2$, the crystal anisotropy $\phi_K = K_1 \sin^2\varphi + K_2 \sin^4\varphi$, the stray field energy $\phi_S = -1/2\, \boldsymbol{H}_S \cdot \boldsymbol{J}_S$ and the magnetostatic energy $\phi_H = -\boldsymbol{H}_{ext} \cdot \boldsymbol{J}_S$ (φ: angle between the c-axis and $\boldsymbol{J}_S$, $\boldsymbol{H}_S$: stray field which follows from a scalar potential U by $\boldsymbol{H}_S = -\nabla U$ and U obeys Poisson's equation $\Delta U = \mathrm{div}\boldsymbol{J}_S$). For performing the minimization the Finite Element technique (FEM) is used (Schrefl et al. 1994a; Fischer et al. 1996); that is, the continuum is discretized by the corners of an assembly of triangles (two-dim systems) (Schrefl et al. 1993, 1994a) or tetrahedra (three-dim systems) (Schrefl et al. 1994b; Fischer et al. 1996). In order to obtain the true energy minimum of the magnetic state, the mesh size of the finite elements has to be accommodated to the gradients of $\boldsymbol{J}_S$ and therefore to the $\boldsymbol{J}_S$ distribution. As an example Fig. 13a shows a two-dimensional plot with vanishing mesh length near the grain boundary (Kronmüller et al. 1997). As the basis of the numerical calculations, usually a cubic particle consisting of polyhedral irregular or regular grains is considered. By varying the average grain size, by modifying the magnetic material parameters within the grain boundaries and by forming composite magnets with different amounts of soft magnetic grains, this model allows a systematic study of the main influences on the characteristic properties of the hysteresis loop.

As an example, Fig. 13b shows the distribution of the spontaneous polarization in the remanent state within a model composite magnet – a cube composed of 35 irregular grains with an average grain diameter of 10 nm with the easy axes distributed isotropically and with an amount of 51% soft magnetic α-Fe grains embedded in 49% hard magnetic grains of $Nd_2Fe_{14}B$ (Fischer et al. 1995). It can be clearly seen how the local distribution of the magnetic moments is smoothed at the boundaries of the grains. Under the assumption of a perfect exchange coupling between the grains, Fig. 13c illustrates the dependence of J_R, $\mu_0 H_C$ and $(BH)_{max}$ on the grain size D obtained by means of FEM for the irregular grain structure of Fig. 13b and also for a hypothetical regular structure composed of 35 dodecahedral grains (Kronmüller et al. 1994). All three quantities, in general, decrease with increasing grain size, whereby the regular grain distribution leads to larger values of J_R and $\mu_0 H_C$. The remanence and the coercive field can be fitted empirically by the following logarithmic laws (Fischer et al. 1996):

$$J_R = J_{sat}(0.84 - 0.085 \ln(D/\delta_B^{hard}) \quad (4)$$

$$H_C = H_N(0)(0.22 - 0.04 \ln(D/\delta_{hard}^B) \quad (5)$$

with $H_N(0) = 2K_1^{hard}/J_S$ and $J_{sat} = J_S^{hard} v^{hard} + J_S^{soft} v^{soft}$, where the upper indices refer to the saturation polarizations and volume fractions of the hard and soft magnetic phases. It turns out that for grain sizes of 20 nm, i.e. $5\,\delta_B^{hard}$, the coercive field is of the order of 15% of the ideal coercive field $H_N(0) = 2K_1^{hard}/J_S$ and the remanence enhancement is far above the isotropic value of $J_R/J_S = 0.5$. In Fig. 13d the numerical results obtained for the three characteristic properties of the hysteresis loop as a function of the α-Fe content (Fischer et al. 1995) are compared with the corresponding experimental data achieved for NdFeB (Willcox et al. 1994; Bauer et al. 1996) and PrFeB (Goll et al. 1998) composite magnets. (The dotted line represents the case of non-interacting and randomly distributed grains). Whereas the numerical results for the remanence agree fairly well with the experimental data, the theoretical prediction of H_C and $(BH)_{max}$ lies appreciably over the experimental values. In the case of $(BH)_{max}$ this is due to the fact that for our experimental results the condition $\mu_0 H_C > 0.5 J_R$ is valid for α-Fe concentrations smaller than 30% whereas the numerical results fulfil this condition up to 50% α-Fe. The observed discrepancy between the experimental and numerical results can be eliminated if the influence of the grain boundaries is no longer ignored. Within a grain boundary all three intrinsic material parameters J_S, A and K_1 may be submitted to modifications. Due to the atomic disorder we may assume that in particular A and K_1 have reduced values within a grain boundary (modifications of J_S would lead to completely controversial results (Fischer and Kronmüller 1996). Fig. 13e shows the influence of a reduction of these two material parameters on the demagnetization curves for a cube of 64 grains with an average diameter of 20 nm (Fischer and Kronmüller 1998). For the model calculation the grain boundaries were presumed to have an intergranular width of 3 nm wherein the material constants A and K_1 suffer a step-like reduction. Accordingly, with decreasing exchange constant and crystal anisotropy within the grain boundaries both properties, $\mu_0 H_C$ and J_R, decrease smoothly. If we introduce the parameter f defined as the ratio $f = A^{gb}/A = K_1^{gb}/K_1$, where A^{gb} and K_1^{gb} denote the material parameters within the grain boundary, the coercive field and the remanence standardized to the nucleation field $H_N(0) = 2K_1^{hard}/J_S$ and the saturation polarization J_{sat}, respectively, can be written as (Fischer and Kronmüller 1998):

$$H_C/H_N(0) = 0.304 + 0.098f \quad (6)$$

$$J_R/J_{sat} = 0.646 + 0.036f \quad (7)$$

A further interesting property is the dependence of the coercive field as a function of the average grain size $\langle D \rangle$. Here it turns out that for an understanding of the experimental results obtained by Manaf et al. (1991) for nanocrystalline $Nd_{13.2}Fe_{79.6}B_6Si_{1.2}$ the modifications of A and K_1 within the grain boundary are able to describe the experimental results rather nicely (*diamonds* in Fig. 13f) (Kronmüller et al. 1997). Fig. 13g shows the corresponding magnetization reversal process by plotting the magnetization reversal for an individual grain

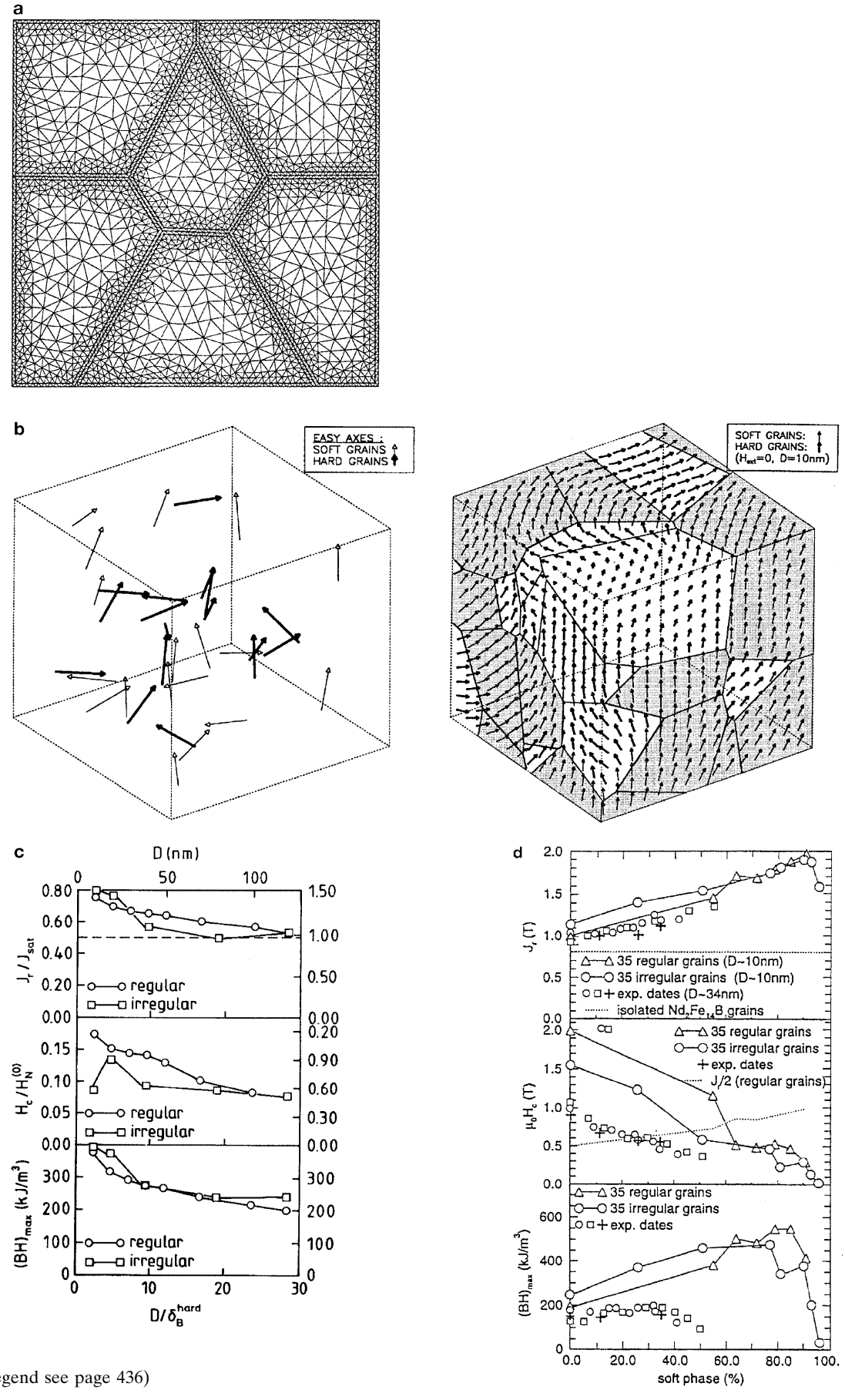

Fig. 13 (Legend see page 436)

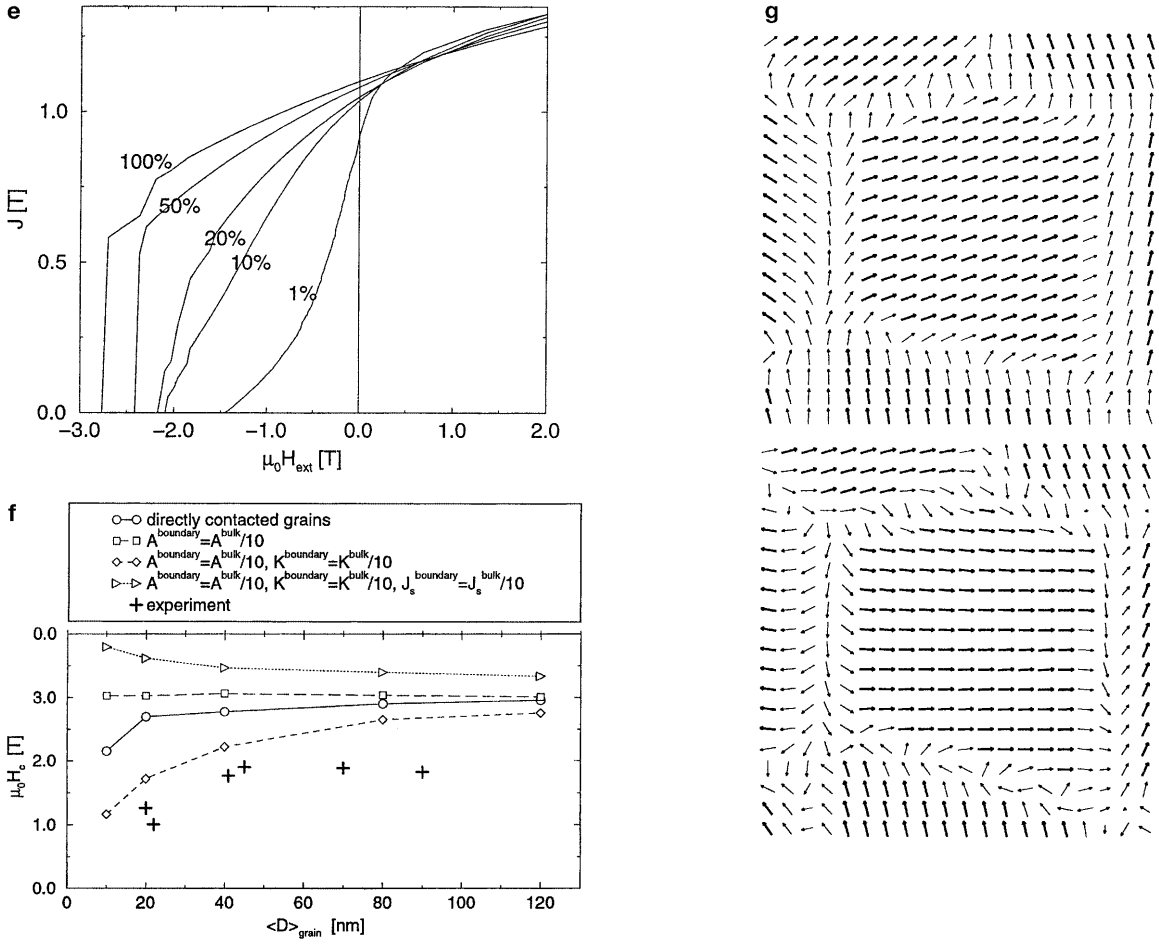

Fig. 13 **a** The finite-element mesh showing the refinement of the mesh length near the grain boundaries: Inside the grains the mesh length is chosen to be about 1/20 of the grain size and near the grain boundaries the ratio amounts to about 1/100. The smallest absolute mesh length is 1 nm. **b** Configurations of the easy axes (*left*) and the remanent polarization (*right*) of 35 irregular grains of average diameter 10 nm within a cube with a volume fraction of 51% α-Fe (*dark*) and 49% $Nd_2Fe_{14}B$ (*light*). **c** Remanence J_R, coercivity $\mu_0 H_C$ and maximum energy product $(BH)_{max}$ for the irregular configuration of Fig. 13b and a regular dodecahedral grain structure as a function of the grain size D. **d** Numerical results for J_R, $\mu_0 H_C$ and $(BH)_{max}$ of nanocrystalline composite magnets for regular and irregular distributions of grains (average grain size 10 nm) as a function of the amount of the α-Fe phase. Experimental results: + (Willcox et al. 1994), o (Bauer et al. 1996), □ (Goll et al. 1998). **e** Demagnetization curves for an ensemble of 64 NdFeB grains of an average grain diameter of 20 nm and an intergranular phase of 3 nm thickness. The percentages refer to the relative reduction of the exchange constant and the anisotropy constant within the intergranular phase. **f** Coercive field as a function of the mean grain diameter of grains with isotropically distributed easy axis and grain boundaries of width 3 nm. **g** *Top*: magnetization distribution at the remanent state. *Bottom*: magnetization distribution at the overcritical state just before magnetization reversal. The *strong arrows* indicate the magnetic moments within the bulk of the grain

separated from neighbouring grains by a grain boundary with reduced values of the exchange and the magnetocrystalline constant (Kronmüller et al. 1997). Here it is evident that the reversal of magnetization primarily takes place within the grain boundary and the neighbouring regions, whereas in the bulk of the grain the magnetization just starts to rotate into the direction of the magnetic field.

References

Bauer J, Seeger M, Zern A, Kronmüller H (1996) Nanocrystalline NdFeB permanent magnets with enhanced remanence. J Appl Phys 80:1667–1673

Brown WF Jr (1945) Virtues and weaknesses of the domain concept. Rev Mod Phys 17:15–19

Buschow KHJ (1988) Permanent magnet materials based on 3d-rich ternary compounds. In: Wohlfarth EP, Buschow KHJ (eds) Ferromagnetic materials, vol 4. North Holland, Amsterdam, pp 1–130

Buschow KHJ (1997) Magnetism and processing of permanent magnet materials. In: Buschow KHJ (ed) Handbook of magnetic materials, vol 10. North Holland, Amsterdam, pp 463–593

Chen J, Kronmüller H (1990) Properties of NdFeB magnets processed by the hydrogen decrepitation technique. Phys Stat Sol (A) 120:617–626

Chen CH, Walmer MS, Walmer MH, Liu S, Kuhl E, Simon G (1998) $Sm_2(Co,Fe,Cu,Zr)_{17}$ magnets for use at temperatures $\geq 400\,°C$. J Appl Phys 83:6706–6708

Coey JMD, Sun H (1990) Improved magnetic properties by treatment of iron-based rare earth intermetallic compounds in ammonia. J Magn Magn Mater 87:251–254

Croat JJ, Herbst JF, Lee RW, Pinkerton FE (1984) Pr–Fe and Nd–Fe based materials: A new class of high performance permanent magnets. J Appl Phys 55:2078–2082

Fidler J (1992) Two types of dopants with different microstructural effects leading to an improvement of rare earth-iron based permanent magnets. In: Street B (ed) Proceedings of the 7th international symposium in magnetic anisotropy and coercivity in RE-TM alloys. University of Western Australia, Perth, p. 11-22

Fischer R, Kronmüller H (1996) Static computational micromagnetism of demagnetization processes in nanoscaled permanent magnets. Phys Rev B 54:7284–7294

Fischer R, Kronmüller H (1998) The role of grain boundaries in nanoscaled high-performance permanent magnets. J Magn Magn Mater 184:166–172

Fischer R, Schrefl T, Kronmüller H, Fidler J (1995) Phase distribution and computed magnetic properties of high-remanent composite magnets. J Magn Magn Mater 150:329–344

Fischer R, Schrefl T, Kronmüller H, Fidler J (1996) Grain-size dependence of remanence and coercive field of isotropic nanocrystalline composite permanent magnets. J Magn Magn Mater 153:35–49

Goll D, Kronmüller H (1998) Nanocrystalline PrFeB based permanent magnets with enhanced remanence. In: Schultz L, Müller KH (eds) Proceedings of the 15th international workshop on REM and their applications, Dresden Werkstoff-Informationsgesellschaft, Frankfurt, pp 189–198

Goll D, Seeger M, Kronmüller H (1998) Magnetic and microstructural properties of nanocrystalline exchange coupled PrFeB permanent magnets. J Magn Magn Mater 185:49–60

Goll D, Kleinschroth I, Kronmüller H (2000a) High-Perfomance Nanocrystalline PrFeB-Based Bonded Permanent Magnets. In: Kaneko H, Homma M, Okada M (eds) Proceedings of the 16th international workshop on REM and their applications, Sendai, the Japan Institute of Metals, pp 641–650

Goll D, Kleinschroth I, Sigle W, Kronmüller H (2000b) Melt-spun precipitation-hardened $Sm_2(Co,Cu,Fe,\ Zr)_{17}$ magnets with abnormal temperature dependence of coercivity. Appl Phys Lett 76:1054–1056

Gong W, Hadjipanayis GC, Krause RI (1994) Mechanically alloyed nanocomposite magnets. J Appl Phys 75:6649–6651

Hadjipanayis GC (1999) Nanophase hard magnets. J Magn Magn Mater 200:373–391

Hadjipanayis GC, Hazleton RC, Lawless KR (1984) Cobalt-free permanent magnet materials based on iron-rare-earth alloys. J Appl Phys 55:2073

Harris IR (1996) Magnet processing. In: Coey JMC (ed) Rare-earth iron permanent magnets. Clarendon, Oxford, pp 336–380

Henig ET, Grieb B (1991) Phase diagrams for permanent magnet materials. In: Long GJ, Grandjean F (eds) Supermagnets, hard magnetic materials. Kluwer, Dordrecht, p. 171–226

Herbst JF (1991) $R_2Fe_{14}B$ materials: intrinsic properties and technological aspects. Rev Mod Phys 63:819–898

Hund F (1925) Atomtheoretische Deutung des Magnetismus der seltenen Erden. Z Phys 33:855–859

Kneller E (1962) Ferromagnetismus. Springer, Berlin Heidelberg New York

Kneller EF, Hawig R (1991) The exchange-spring magnet: a new material principle for permanent magnets. IEEE Trans Magn 27:3588–3600

Kojima H (1982) Fundamental properties of hexagonal ferrites with magnetoplumbite structure. In: Wohlfarth EP (ed) Ferromagnetic materials, vol 3. North Holland, Amsterdam, pp 305–392

Kools F (1992) Hard Ferrites. In: Evetts J (ed) Magnetic and Superconducting Materials. Pergamon Press, Oxford, New York, Seoul, Tokyo:129–135

Kou XC, Kronmüller H, Givord D, Rossignol MF (1994) Coercivity mechanism of sintered $Pr_{17}Fe_{75}B_8$ and $Pr_{17}Fe_{53}B_{30}$ permanent magnets. Phys Rev B 50:3849–3860

Kronmüller H (1978) Micromagnetism in hard magnetic materials. J Magn Magn Mater 7:341–350

Kronmüller H (1987) Theory of nucleation fields in inhomogeneous ferromagnets. Phys Stat Sol (B) 144:385–396

Kronmüller H (1991) Micromagnetic background of hard magnetic materials. In: Long GJ, Grandjean F (eds) Supermagnets, hard magnetic materials. Kluwer, Dordrecht, pp 461–498

Kronmüller H, Durst KD, Ervens W, Fernengel W (1984) Micromagnetic analysis of precipitation hardened permanent magnets. IEEE Trans Magn 20:1569–1571

Kronmüller H, Durst KD, Sagawa M (1988) Analysis of the magnetic hardening mechanism in REFeB permanent magnets. J Magn Magn Mater 74:291–302

Kronmüller H, Schrefl T, Fischer R, Fidler J (1994) Micromagnetic analysis of coercivity of rare earth-transition metal intermetallics and interstitial compounds. In: Manwaring CAF, Jones D, Williams A, Harris I (eds) Proceedings of the 8th international symposium on magnetic anisotropy and coercivity in RE-TM alloys. University of Birmingham, Birmingham, UK, pp 1–24

Kronmüller H, Fischer R, Seeger M, Zern A (1996) Micromagnetism and microstructure of hard magnetic materials. J Phys D 29:2274–2283

Kronmüller H, Fischer R, Hertel R, Leineweber T (1997) Micromagnetism and the microstructure in nanocrystalline materials. J Magn Magn Mater 175:177–192

Kronmüller H, Goll D, Kleinschroth I, Zern A (1999) Hysteresis loops and coercivity mechanisms in sintered and nanocrystalline permanent magnets. Mat Res Soc Symp Proc 577, Materials Research Society:303–314

Kumar K (1988) $RETM_5$ and RE_2TM_{17} permanent magnets development. J Appl Phys 63:R13–R57

Liu JF, Zhang Y, Ding Y, Dimitrov D, Hadjipanayis GC (1998) Rare earth permanent magnets for high temperature applications. In: Schultz L, Müller KH (eds) Proceedings of the 15th international workshop on REM and their applications, Dresden. Werkstoff-Informationsgesellschaft, Frankfurt, pp 607–622

Manaf A, Buckley RA, Davies HA, Leonowicz M (1991) Enhanced magnetic properties in rapidly solidified NdFeB based alloys. J Magn Magn Mater 101:360–362

Manaf A, Al-Khafaji MA, Zhang PZ, Davies HA, Buckley RA, Rainforth WM (1993) Microstructure analysis of nanocrystalline NdFeB ribbons with enhanced hard magnetic properties. J Magn Magn Mater 128:307–312

Martinek G, Kronmüller H (1990) Influence of grain orientation of the coercive field in FeNdB permanent magnets. J Magn Magn Mater 86:177–183

McCurrie RA (1982) The structure and properties of Alnico permanent magnets. In: Wohlfarth EP (ed) Ferromagnetic materials, vol 3. North Holland, Amsterdam, pp 107–188

Sagawa M, Hirosawa S (1987) Coercivity and microstructure of RFeB sintered permanent magnets. J Phys (Paris) Colloq 49:617–622

Sagawa M, Fujimura S, Togawa N, Yamamoto H, Matsuura Y (1984) New material for permanent magnets on a base of Nd and Fe. J Appl Phys 55:2083–2087

Schneider G, Henig ET, Petzow G, Stadelmeier HH (1986) Phase relations in the system FeNdB. Z Metallkunde 77:755–761

Schrefl T, Kronmüller H, Fidler J (1993) Exchange hardening in nano-structured two-phase permanent magnets. J Magn Magn Mater 127:273–277

Schrefl T, Fidler J, Kronmüller H (1994a) Remanence and coercivity in isotropic nanocrystalline permanent magnets. Phys Rev B 49:6100–6110

Schrefl T, Fidler J, Kronmüller H (1994b) Nucleation fields of hard magnetic particles in 2D and 3D micromagnetic calculations. J Magn Magn Mater 138:15–30

Seeger M, Köhler D, Kronmüller H (1994) Magnetic and microstructural investigations of melt-spun Fe(NdPr)B. J Magn Magn Mater 130:165–172

Shen BG, Kong LS, Wang FW, Cao L (1993) Structure and magnetic properties of $Sm_2Fe_{14}Ga_3C_x$ ($x=0$–2.5) compounds prepared by arc melting. Appl Phys Lett 63:2288–2290

Stoner EC, Wohlfarth EP (1948) A mechanism of magnetic hysteresis in heterogeneous alloys. Phil Trans R Soc, London 240:599–642

Strnat K (1988) Rare earth – cobalt permanent magnets. In: Wohlfarth EP, Buschow KHJ (eds) Ferromagnetic materials, vol 4. North Holland, Amsterdam, pp 131–210

Strnat K, Hoffer G, Olsen JC, Ostertag W, Becker JJ (1967) A family of new cobalt-base permanent magnet materials. J Appl Phys 38:1001–1002

Willcox M, Williams J, Leonowicz M, Manaf A, Davies H (1994) Relations between phase constitution, determined by Mössbauer spectroscopy, and the enhanced magnetic properties for nanocrystalline FeNdB alloys. In: Manwaring CAF, Jones D, Williams A, Harris I (eds) Proceedings of the 8th international symposium on magnetic anisotropy and coercivity in RE-TM alloys. University of Birmingham, Birmingham, UK, pp 87–94

Withanawasam L, Murthy AS, Hadjipanayis GC (1995) Hysteresis behavior and microstructure of exchange coupled $R_2Fe_{14}B/\alpha$-Fe magnets. IEEE Trans Magn 31:3608–3610

Zeppelin F von (1999) Magnetisierungsprozesse in intermetallischen Verbindungen der Seltenerdmetalle. Diploma thesis, Universität Stuttgart

Zern A (1995) Mikrostruktur und magnetische Eigenschaften von nanokristallinen austauschgekoppelten FeNdB Magneten. Diploma thesis, Universität Stuttgart

Zern A, Seeger M, Bauer J, Kronmüller H (1998) Microstructural investigations of exchange coupled and decoupled nanocrystalline NdFeB permanent magnets. J Magn Magn Mater 184:89–94